Available online at www.sciencedirect.com
SCIENCE DIRECT®
Journal of volcanology and geothermal research
ELSEVIER
Journal of Volcanology and Geothermal Research 129 (2004) 83–97
www.elsevier.com/locate/jvolgeores

Experimental observations of the effect of crystals and pre-existing bubbles on the dynamics and fragmentation of vesiculating flows

C.C. Mourtada-Bonnefoi *, H.M. Mader

Department of Earth Sciences, University of Bristol, Wills Memorial Building, Queens Road, Bristol BS8 1RJ, UK

Received 28 June 2002; accepted 22 April 2003

Abstract

The effect of crystals and pre-existing gas phases on the dynamic degassing and fragmentation of magmas in a volcanic conduit have been simulated by analogue experiments. A series of decompression experiments of viscous solutions of gum rosin and acetone with and without the incorporation of particles (silicon carbide, glass beads, organic seeds) or pre-existing air bubbles have been performed in a transparent shock-tube. The addition of internal bubbles or solid particles in the starting solution shifts the fragmentation conditions towards lower acetone (volatile) contents and lower decompression ratios. The effect of solid particles depends on their number density and spatial distribution in the starting solution. A small number of sinking particles has little impact on the flow dynamics. However, a floating layer of particles provides a high concentration of surface bubbles that leads to an early fragmentation pulse. The observations also imply that the presence of crystals, if able to generate a high number density of bubbles, will lead to an earlier and deeper fragmentation of the magma in the volcanic conduit.
© 2003 Elsevier B.V. All rights reserved.

Keywords: degassing; fragmentation; multiphase flow; bubble nucleation; bubble growth; explosive eruptions

1. Introduction

Magma eruptions can produce a wide range of eruptive styles ranging from effusive to explosive volcanism. The dynamic evolution of magmatic multiphase flows at depth in a volcanic conduit is an essential component of the physics of eruptions. During magma ascent in a volcanic conduit, internal gas evolution generates an expanding bubbly flow which, in the case of explosive eruptions, fragments before reaching the surface into a gas-particle flow by rupture of the continuous liquid phase of the silicate magma. One may distinguish the dynamic fragmentation of a magma that is flowing up to the surface in a volcanic conduit from the fragmentation of static volcanic products, such as dome collapse, secondary pyroclastic flows, and popping rocks. The mechanism and the condition for magma fragmentation and thus for an explosive eruption is currently a subject of debate. The fragmentation mechanism, whether static or dynamic, is often described as either brittle or ductile (Dingwell, 1997; Melnik, 1999; Papale,

* Corresponding author.
E-mail addresses: c.mourtada@wanadoo.fr (C.C. Mourtada-Bonnefoi), h.m.mader@bristol.ac.uk (H.M. Mader).

0377-0273/03/$ – see front matter © 2003 Elsevier B.V. All rights reserved.
doi:10.1016/S0377-0273(03)00233-6

1999; Sahagian, 1999; Zhang, 1999). Fragmentation is thought to occur at a critical film thickness in the case of ductile fragmentation (Proussevitch et al., 1993) and depends on parameters such as strain rate or gas overpressure in the bubbles in the case of brittle fragmentation (Melnik, 1999; Papale, 1999). In the case of degassing and decompression in a volcanic conduit, magma fragmentation thus depends on parameters that are evolving dynamically. As a result, the determination of the instant and the depth of fragmentation in a conduit also depends on our understanding of the previous bubbly flow dynamics.

A major complication to the physics of magmatic bubbly flows is the evolution of the properties of the liquid phase as degassing proceeds. Indeed, the viscosity of the liquid phase increases by up to 7 orders of magnitude as volatile is progressively lost to the bubbles. Strong gradients in viscosity occur spatially due to volatile-depleted and so highly viscous skins around bubbles (Mourtada-Bonnefoi and Mader, 2001). The gas diffusivity in the melt is also a strong function of volatile content. This complex coupling of liquid viscosity, diffusivity and degassing kinetics (Proussevitch and Sahagian, 1998; Blower, 2001; Blower et al., 2001b; Lensky et al., 2001) must play a major role in bubbly flow dynamics and thus has implications for the conditions of dynamic fragmentation.

Direct observation of the dynamic fragmentation process in the field is impossible due to the hazard involved and because it often occurs at depth within the volcanic conduit. As a result, the improvement of our understanding of the physics of magma flow comes from numerical modelling and from physical laboratory experiments that investigate the fundamental processes that operate during such gas-driven explosions. The studies of Alibidirov and Dingwell (1996a,b) and Martel et al. (2000, 2001) have focussed on the brittle fragmentation of porous material. Flow dynamics and fragmentation have been studied by Hill and Sturtevant (1990), Mader et al. (1994, 1996, 1997) and Sugioka and Bursik (1995). All of these studies use analogue (i.e. non-magmatic) materials. In most cases, the studies are restricted to a consideration of the fragmentation of two-phase, liquid-gas systems. The exception to this is the study of Sugioka and Bursik (1995) who considered the vaporisation of a volatile liquid in which inert particles were suspended (i.e. theirs is a three-phase system with just two chemically-distinct components). But natural magma flows generally involve at least three chemically-distinct phases: a liquid, a gas phase and crystal phases. In this paper, we present a study of dynamic fragmentation caused by internal gas evolution in an analogue system that involves three chemically-distinct phases. The fragmentation processes observed in the experiments discussed here therefore incorporate most of the key features of the complex natural multiphase flow dynamics.

2. The analogue materials

The experiments were performed using solutions of gum rosin and acetone (GRA) as the continuous phase. Gum rosin is an organic compound composed mainly of $C_{19}H_{29}COOH$ and derives from the dehydration of natural pine resins (Cobbold and Jackson, 1992). It is soluble in most organic solvents including acetone. The use of the GRA chemical system as an analogue of magmas is motivated by several of its properties. First, GRA solutions degas violently during decompression below atmospheric pressure. Second, the viscosity and volatile diffusivity response to degassing of GRA solutions is similar to that of hydrated felsic magmas (Phillips et al., 1995; Blower, 2001). These features are discussed in more detail in Sections 2.1 and 2.2. Finally, the GRA foams produced by the experiments behave as a weak solid and so can be sampled and their texture studied (Blower et al., 2001a).

As an analogue of crystals in magmas (the discontinuous phase), we used a range of solid particles of different nature, shape and size (Table 1): silicon carbide particles, glass spheres and organic seeds (mustard, coriander and other seeds). The surface properties differ among particles. The organic seeds have a rougher surface than either the silicon carbide or the glass particles: the mustard seeds are spherical but covered with tiny hairs; the coriander seeds have an ovoid shape and a

Table 1
Characteristics of the solid particles added to the GRA starting solutions

Nature	Shape	Size	Density (kg m^{-3})	Other comments
Silicon carbide	Angular, smooth faces	100 μm long	3200	Sinking
Glass	Spherical, smooth surface	0.5–3 mm diameter	2500	Sinking
Mustard seeds	Spherical, hair covered	1–2.5 mm diameter	1100	Sinking
Coriander seeds	Ovoid, furrowed surface	5 mm long	1100	Floating

furrowed surface; the silicon carbide particles are angular; the glass particles are smooth spheres. All the particles used sunk into the starting GRA solution to form a bottom layer of particles apart from the coriander seeds which floated at the top of the solutions (Table 1). In every case, the solid particles tended to trap a few tiny air bubbles on their surface when stirred into a GRA solution. After decompression, these air bubbles grow and contribute to the flow. Furthermore, the particles were observed to induce continuous heterogeneous bubble nucleation on their surface, with the sole exception of the silicon carbide particles.

Violent degassing and fragmentation of these solutions is generated by imposing a sudden decompression by bursting a diaphragm separating a test-cell containing the analogue solution from a shock-tube and vacuum chamber, as shown in Fig. 1.

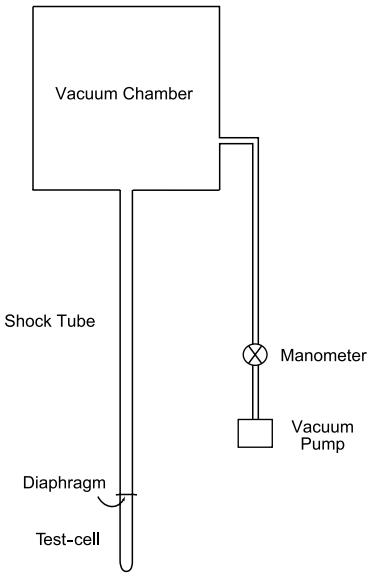

2.1. GRA degassing behaviour

The decompression of a GRA solution induces degassing by acetone boiling. As a consequence, at a fixed temperature, bubbles nucleate in GRA solutions at pressures below the acetone boiling point. A series of instantaneous decompression experiments from 10^5 Pa to various low pressures in the range of 10^4–3.5×10^4 Pa were conducted at room temperature in the shock-tube using pure acetone and GRA solutions of 20, 25 or 30 wt% acetone. We observed that bubbles nucleated at room temperature below the pressure of 1.98×10^4 Pa in both pure acetone and in GRA solutions (Fig. 2). From these results we infer that the dissolution of the solid organic compound of

Fig. 1. Experimental apparatus. The vacuum chamber is a metallic cylinder with a capacity of 0.2 m^3 that is connected to a vacuum pump working in the pressure range of 10^5–10 Pa. The pressure line between the pump and the chamber holds a Bourdon gauge indicating pressures below 5000 Pa, a pressure valve connected to the atmosphere and a valve opening or closing the connection with the vacuum chamber. The vacuum chamber stands at 2 m height above the floor and has a 1-m-long shock-tube below it. The connection of the shock-tube to the vacuum chamber is made through an aluminium plate designed to avoid pressure leaks, but which can be removed easily to clean the vacuum chamber. The diaphragm assembly separates the shock-tube from the test-cell and has an internal diameter of 4 cm, the same as the shock-tube. It consists of a PTFE ring, around which a Nickel-Chrome resistance wire runs, circling most of its internal diameter. The diaphragm is made of a thick adhesive tape that is stuck to the diaphragm assembly in contact with the circle wire. By passing around 10 A of current, the heat of the wire melts the tape and the diaphragm then bursts because of the pressure differential across it. The test-cell is a cylindrical pyrex tube of 4 cm internal diameter sealed at one extremity and presenting a smoothly rounded surface. This test-cell is 25 cm long, 0.4 cm thick and entirely transparent.

gum rosin into liquid acetone does not affect the boiling point of the system, and that the phase diagram of the GRA system is identical to that of pure acetone. Following the crossing of its boiling point during decompression, acetone undergoes a phase transition from a liquid to a gas.

The degassing process of the GRA system differs from that of hydrated magmas that degas by volatile exsolution from the magmatic liquid. We now discuss the differences and similarities of these two degassing processes. Magmatic melts are characterised by a saturation curve in volatiles. This property describes the pressure conditions of the equilibrium between the magmatic liquid and a gas phase. This contrasts with acetone that can be in equilibrium either as a liquid or as a gas phase. In the GRA system, the coexistence of a liquid and an acetone gas phase can only occur during acetone phase transitions.

The condition for bubble nucleation in magmas is the excess of an oversaturation pressure threshold. By contrast, the condition for acetone bubble nucleation in the GRA system is the crossing of the acetone boiling point. Magma oversaturation pressure threshold depends on the liquid volatile content or on pressure whereas the acetone boiling point is independent of liquid gum rosin

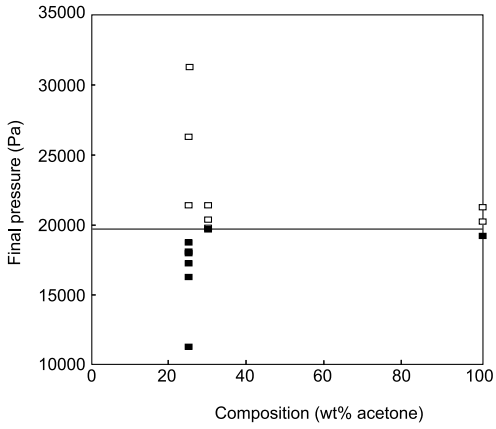

Fig. 2. Bubble nucleation conditions in the GRA solutions at room temperature. After rapid decompression of the GRA solutions to a final pressure, we either observed surface bubbling (black squares) or no bubbling (hollowed squares). As a result, the condition for bubble nucleation in the GRA system and in pure acetone is that the final pressure has to be below 1.98×10^4 Pa.

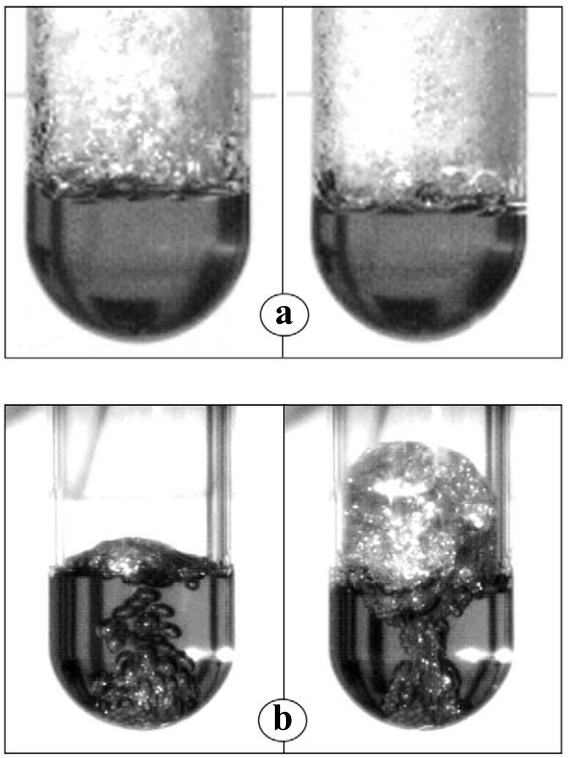

Fig. 3. Bubble nucleation sites. (a) Surface nucleation of bubbles in GRA particle-free and bubble-free solutions. The nucleation surface propagates downwards at a constant velocity. The images are from run 45; the second image was taken 1000 ms after the first one. In this run, the velocity of the nucleation surface is about 4 mm s^{-1}. (b) Internal bubble nucleation in particle-bearing solutions. Example of nucleation on a sinking layer of mustard seeds.

content. As a result, bubble nucleation proceeds continuously in a decompressed GRA solution whereas in magmas bubble nucleation can rapidly stop because of degassing-driven depletion in volatile of the liquid.

Another difference in the bubble nucleation process in the two systems is that bubble nucleation is internal in magmas whereas it only occurs on the surface of particle-free GRA solutions (Fig. 3), as in pure superheated liquids (e.g. Hill and Sturtevant, 1990). However, in particle-bearing GRA solutions, internal bubble nucleation also occurred.

The driving force for bubble growth in magmas is the oversaturation pressure, that is the pressure difference between the local pressure and satura-

tion pressure, whereas in the GRA system it is the pressure difference between the final ambient pressure and acetone boiling pressure. In this respect, the boiling pressure in a GRA solution can be taken as analogous to the saturation pressure in magmas.

Additionally, bubble growth dynamics can be compared in chemical systems because in both cases bubble growth may be affected by diffusion of the volatile from the liquid and by the viscous resistance of the surrounding liquid.

2.2. Viscosity and acetone diffusivity of GRA solutions

The rheological properties of GRA solutions is one of the major reasons for the use of this system as an analogue of magmas. Table 2 and Fig. 4 show measurements of the viscosity of GRA solutions over the range of composition and temperature of the starting conditions for our shock-tube experiments.

The diffusion coefficient of acetone in the GRA solutions was measured by a mass-loss method (Blower, 2001). A thin film of 1 mm thick of GRA solution of known acetone content was poured into a shallow dish of 9 cm diameter and placed on a mass balance in a fume cupboard. Acetone evaporates from the free surface of the film and the mass of the film is measured over a period of a few hours. The mass loss rate is controlled by the rate at which acetone diffuses to the free surface of the film. The diffusivity of acetone in GRA solutions increases with acetone content and therefore varies with time and position in the film. The measurements therefore provide an average value of diffusivity over the range of concentrations present in the film during the experiment. Typical average diffusivities are of the order of 10^{-11} m^2 s^{-1} at 20°C, which is comparable to the diffusivity of water in rhyolitic magmas.

3. Experimental method

The experimental apparatus used is shown in Fig. 1. The GRA solution is prepared by dissolving a known weight of solid gum rosin into a known weight of liquid acetone in a continuously stirred and sealed glass flask. Solutions were prepared the same day or the day before a given run

Table 2
Viscosity of gum rosin–acetone solutions. The viscosity of GRA solutions is a strong function of acetone content X and temperature T. The viscosity measurements are from Phillips et al. (1995) in the top part of the table ($0 \le X \le 20$ wt% acetone) and from this study in the bottom part of the table ($20 \le X \le 30$ wt% acetone). Our solutions containing 20, 25 and 30 wt% acetone were prepared by dissolving, at room temperature and in a closed flask, a known weight of gum rosin powder in a known weight of liquid acetone. The rheology of these solutions was determined using a Haake RV20 rotary viscometer. Previous calibration of the viscometer with silicon oil of known viscosity showed the error on the measured viscosity was $<4\%$. The solutions were all Newtonian. The viscosity of GRA solutions containing 20 wt% acetone was consistent with previous measurements (Phillips et al., 1995), despite the use of a different batch of gum rosin. The viscosity η of the GRA liquid can be fitted by $\log_{10}\eta = -15+(8203.9-618.39X+41.693X^2-1.3446X^3+0.0162X^4)/T$, where η is in Pa.s, X is in wt% acetone and T in K. The values of viscosity calculated using the above formula are given for comparison in the last column. The formula gives a good approximation of GRA viscosity at temperatures between 15 and 30°C in the complete composition range (Fig. 4). At temperatures above 30°C this formula applies only to compositions with 15–30 wt% acetone

X (wt% acetone)	T (°C)	η (Pa.s measured)	η (Pa.s calculated)
0	20	10^{13}	10^{13}
12	20	19	24.01
15	20	6.5	4.67
15	20	2.5	4.67
20	20	0.5	0.69
0	35.5	8.91 10^8	3.91 10^{11}
0	26.6	1.6 10^{11}	2.41 10^{12}
12	59.2	0.30	0.28
12	20.7	19.50	21.9
15	44.3	0.30	0.29
15	3.2	46.77	41.91
20	39.1	0.13	0.09
20	10.1	1.12	2.29
20	20	0.814	0.694
25	20	0.159	0.116
25	20	0.112	0.116
30	20	0.045	0.043
20	25	0.498	0.391
25	25	0.093	0.067
30	25	0.040	0.025

in order to avoid acetone loss. For the same reason, the dissolution was performed at room temperature except for the most resin-rich solutions (15% acetone) which were heated to obtain homogeneity. A given weight of solution was poured into the test-cell, quickly sealed by the diaphragm and fixed to the shock-tube. In the case of particle-bearing experiments, the solid particles were poured into the solution in the test-cell at this stage. To avoid undesired heterogeneous nucleation on its internal surface, the test-cell was previously cleaned meticulously with acetone. The solution was left in the test-cell for 20–30 min to ensure equilibrium with room temperature and to allow air bubbles to ascend to the surface of the solution and burst. This procedure successfully removed all air bubbles from the pure GRA runs but in the particle-bearing runs a few air bubbles remained attached to the sinking particles.

The pressure above the diaphragm was lowered to the desired pressure using the vacuum pump and maintained at that pressure by regulating the opening of a pressure valve. An experiment consisted of the rapid decompression of the analogue solution from atmospheric pressure by bursting the diaphragm. Decompression induced the nucleation and growth of bubbles in the analogue solution and thus generated a flow, which propagated up the transparent tube and was recorded using a high-speed video camera at framing rates up to 1000 frames per second.

The images were analysed to derive the height of the front of the flow as a function of time. The measurements were made for the initial bubbly flow. After fragmentation, the position of the flow front could no longer be clearly identified on the frames: pulses of acetone vapour make any attempt of measurement very hazardous. After each run, the final height reached by the front of the flow or by foamy fragments was measured. In some runs, the partially degassed GRA solution in the shock-tube was sampled to estimate its acetone content by measuring the weight loss of the solution in a furnace at 90°C after 24 h. From this estimate we derived the mean viscosity of this sample given the previously established relationship between the viscosity of a GRA solution and its acetone content (see Table 2 and Fig. 4). This method allowed us to quantify variations of the mean viscosity of the liquid at the front of the foamy end-products for a few experiments. In the fragmenting runs, no direct measurements could be performed prior fragmentation because no sampling can be done during the course of a run.

4. Experimental results

4.1. Particle- and bubble-free runs

In the absence of air bubbles or particles, the GRA system produces a range of flow behaviour and end-product texture. Images of these textures have been published by Blower et al. (2002). The GRA flows all start with a bubbly flow characterised by an exponential propagation law (Mourtada-Bonnefoi and Mader, 2001): $h \propto e^{at}$ where h is

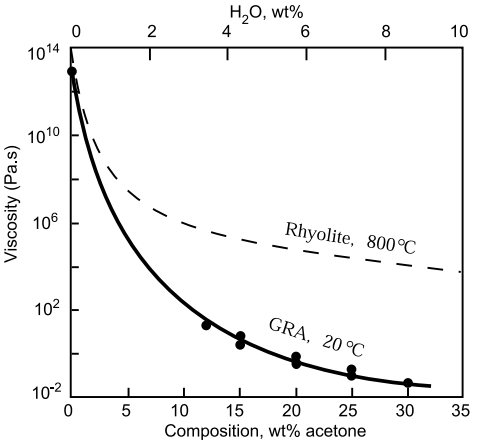

Fig. 4. Viscosity of gum rosin–acetone solutions. GRA liquids have a viscosity that is a strong function of acetone concentration and temperature. Data for acetone concentration $X = 0$–20 wt% acetone from Phillips et al. (1995) are here combined with our data for $X = 20$–30 wt% acetone (Table 2) to derive an empirical formula for the viscosity η in Pa.s as a function of acetone content X in wt% and temperature T in K: $\log_{10}\eta = -15 + (8203.9 - 618.39X + 41.693X^2 - 1.3446X^3 + 0.0162X^4)/T$. This formula gives a good approximation of GRA viscosity at temperatures between 15 and 30°C in the complete composition range (compare solid line and data points at 20°C). The viscosity of a rhyolitic magma at 800°C, as a function of its water content (Shaw, 1963), is also given for comparison (dashed line).

the distance of propagation of the flow front and t is time. The coefficient a is constant and can be calculated as the rate of change of vertical velocity $v = dh/dt$ with distance up the conduit: $a = dv/dh$. After fragmentation, we could not identify the position of the flow front and thus could not characterise the flow dynamics of the subsequent gas and fragments flow. The acceleration observed in the initial bubbly flow suggests a diffusion-driven but viscosity-limited bubble growth regime (Mourtada-Bonnefoi and Mader, 2001). By comparison, a diffusion-limited bubble growth regime is expected to result in flow deceleration (e.g. Navon et al., 1998). The exponential coefficient a depends on the run conditions: the higher the starting acetone content X_o and the lower the final pressure P_f, the larger is the coefficient a. More energetic bubbly flows are characterised by a higher coefficient a, shorter run times, more degassed end-products and an increased likelihood of fragmentation.

Fig. 5 shows our data and those presented by Phillips et al. (1995). The uncertainty in the value of a can be estimated from our three repeated runs for 20 wt% initial acetone content, 5000 Pa final pressure, at the temperature of 19.0°C and with a similar starting mass of solution of about 40 g. For these runs a was found to be 7.8, 11.0 and 11.3 s^{-1}, giving a mean value of 10.0 s^{-1} with an uncertainty of $\pm 16\%$ (1σ). This uncertainty is also consistent with the repeat measurements at 25 wt% initial acetone content and 10 000 Pa final pressure. We observe good overlap between our data and those derived from Phillips et al. (1995). We can therefore use the combined dataset to propose an empirical law to estimate the coeffi-

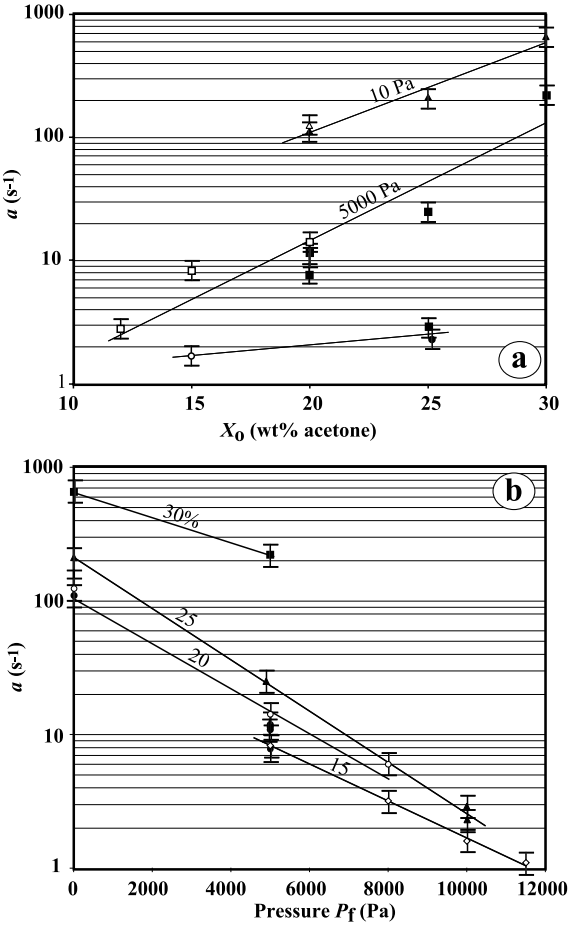

Fig. 5. Variations of the exponential coefficient a. The white data points are the values of the exponential coefficient a that we derived from Phillips et al.'s (1995) runs. The black data points are from this study. In this figure, only our data points for a starting mass of solution of 38.7–40.3 g at a temperature of 19.0–21.0°C are plotted. The spread in our data can be mostly explained by the variations in the starting mass of solution and the temperature variations (Fig. 6). For similar starting conditions the uncertainty on a for our data is estimated to be $\pm 16\%$ (see the text for more details). Three data points derive from the initial bubbly flow of a later fragmenting run (the two runs with 30 wt% initial acetone content and the run with $X_o = 25$ wt% acetone and $P_f = 10$ Pa). The other data are from non-fragmenting runs. (a) Variation of a as a function of the initial composition X_o. The selected data points are for final pressures of 10 000 Pa (spheres), 5000 Pa (squares) and 10 Pa (triangles). The set of data indicates an increase of the coefficient a from the order of 1 to the order of 100 when the final pressure decreases from 10 000 to 10 Pa. Linear regressions between $\log_{10}a$ and initial composition X_o in wt% acetone give the following relationships: $\log_{10}a = -0.1078 + 0.0208X_o$, for $P_f = 10\,000$ Pa; $\log_{10}a = -0.7450 + 0.0935X_o$, for $P_f = 5000$ Pa; $\log_{10}a = +0.5866 + 0.0728\ X_o$, for $P_f = 10$ Pa. (b) Variation of a as a function of the final pressure P_f. The data points are for initial acetone contents of 15 wt% (diamonds), 20 wt% (spheres), 25 wt% (triangles) and 30 wt% (squares). We observe a linear empirical relationship between $\log_{10}a$ and final pressure P_f for a given initial composition X_o. The linear regressions, where a is in s^{-1} and P_f in Pa, are the following: $\log_{10}a = 1.600 - 1.371 \times 10^{-4}\ P_f$, for $X_o = 15$ wt%; $\log_{10}a = 2.006 - 1.180 \times 10^{-4}\ P_f$, for $X_o = 20$ wt%; $\log_{10}a = 2.330 - 1.917 \times 10^{-4}\ P_f$, for $X_o = 25$ wt%; $\log_{10}a = 2.816 - 0.939 \times 10^{-4}\ P_f$, for $X_o = 30$ wt%.

Table 3
Summary of run conditions and main results. In the first column, run numbers that start with a '95' are runs from Phillips et al. (1995), all others are from this study. The second column gives details of the starting system as follows: None = particle-free and bubble-free runs; ms = mustard seeds; cs = coriander seeds; vs = mixture of various seeds; gs = glass spheres; sc = silicon carbide; pb = pre-existing bubbles; the quantity of particles is specified either as a number of particles (e.g. 500 ms) or a mass of particles (e.g. 19 g vs). The other columns give the initial acetone content X_o, the initial mass of solution M_o, the room temperature T, the final pressure P_f, the coefficient a as derived from the observed bubbly flow dynamics $h \propto e^{at}$, the initial height of solution h_o, the final height h_f reached by foam products after decompression. In the last column, the occurrence of fragmentation during a run is indicated by 'Yes' or 'No'

Run	Particles	X_o (wt%)	M_o (g)	T (°C)	P_f (Pa)	a (s^{-1})	h_o (cm)	h_f (cm)	Frag?
95–5	None	12	16	20	5000	2.8	3.0	–	No
95–1	None	15	16	25	11500	1.1	3.0	–	No
95–2	None	15	16	20	10000	1.6	3.0	–	No
95–3	None	15	16	20	8000	3.2	3.0	–	No
95–4	None	15	16	20	5000	8.3	3.0	–	No
95–8	None	20	16	20	10000	–	3.0	–	No
95–7	None	20	16	20	8000	6.0	3.0	–	No
95–6	None	20	16	20	5000	14.2	3.0	–	No
95–9	None	20	16	20	10	124	3.0	–	–
54	None	15.4	10.6	19.0	5000	5.2		33	No
81	pb	15.1	38.3	19.0	5000	3.3	–	41.5	No
82	pb	15.1	37.9	19.0	5000	23.3	–	70	No
83	6g vs	15.1	38.7	20.0	5000	4.0	–	–	No
88	pb	15.1	38.3	19.0	1000	5.0	–	37	No
84	6g vs	15.1	38.7	20.0	1000	109	–	36	No
85	6g vs	15.1	37.4	20.5	1000	370	–	48	No
86	10g vs	15.1	36.7	19.7	1000	310	–	65	No
55	5g sc	15.9	38.1	18.5	4930	6.6	–	64	–
56	vs	15.9	36.8	17.0	4940	–	–	71	No
30	None	20.1	43.5	–	5000	12.6	4.45	65	–
31	None	20.1	40.0	–	5000	4.4	4.2	62	–
33	None	20.1	40.1	19.0	5000	11.0	4.2	57	–
39	None	20.1	40.3	20.0	5000	11.6	4.2	40	–
40	None	20.1	39.8	19.0	5000	11.3	4.2	40	–
49	None	20.1	39.4	17.5	5000	5.2	4.2	–	–
57	None	20.0	39.6	16.0	5000	4.5	4.2	26	–
60	None	20.1	38.6	17.0	5000	3.6	4.2	26	–
62	None	20.1	18.4	15.5	5030	3.1	2.6	20.5	–
65	None	20.1	22.1	21.0	5000	10.2	2.9	31	–
66	None	20.1	10.0	19.0	5000	1.9	1.9	20.5	–
67	None	20.1	29.0	18.0	5000	7.6	3.4	23	–
68	None	20.1	19.3	19.5	5000	5.5	2.7	24.7	–
69	None	20.1	38.7	19.0	5000	7.8	4.2	41.5	No
93	None	20.2	39.9	20.5	5000	–	4.2	35	No
90	None	20.4	40.8	20.2	1000	59	4.2	45	No
63	None	20.1	34.6	17.5	10	110	3.9	28	No
29	50 ms	20.3	39.8	–	5000	16.4	–	82	–
32	50 ms	20.1	40.0	–	5000	10.8	–	55	–
34	50 ms	20.1	39.3	18.0	5000	7.9	–	42	–
22	500 ms	20.0	43.0	–	5000	19.6	–	69	–
35	500 ms	20.1	39.4	–	5000	10.8	–	56	–
36	500 ms	20.0	40.6	–	5000	37.1	–	59	Yes
37	500 ms	20.0	40.1	–	5000	16.4	–	62	–
38	500 ms	20.0	39.2	18.0	5000	11.0	–	67	–
61	100 gs	20.1	38.6	15.5	5000	9.4	–	56.5	–

Table 3 (*Continued*).

Run	Particles	X_o (wt%)	M_o (g)	T (°C)	P_f (Pa)	a (s^{-1})	h_o (cm)	h_f (cm)	Frag?
47	500 gs	20.1	39.9	20.0	5000	30.1	–	81	–
58	2g sc	20.0	39.5	16.0	5000	4.5	–	45	–
64	2g sc	20.1	39.4	15.5	5000	–	–	50	–
92	pb	20.4	38.9	20.0	5000	308	–	60	Yes
95	pb	20.2	39.1	21.0	5000	–	–	>126	Yes
94	5g vs	20.2	38.9	21.0	5000	–	–	>126	Yes
59	10g vs	20.0	37.6	12.5	5000	664	–	60	–
89	10g vs	20.4	41.2	20.0	1000	374	–	>126	Yes
91	pb	20.4	39.4	20.5	1000	333	–	>126	Yes
71	None	25.1	39.6	20.5	10000	2.3	4.4	10	No
74	None	25.1	39.5	20.5	10000	2.9	4.35	10	No
50	None	25.0	39.7	22.5	5000	27.5	4.4	26	No
53	None	25.0	39.5	21.0	4900	24.7	4.35	26	No
72	None	25.1	42.7	20.5	5000	11.7	4.6	30	–
79	None	25.0	39.0	17.8	5000	26.6	4.3	26	No
73	None	25.1	39.8	20.0	10	212	4.3	67	Yes
78	50 cs	25.0	38.5	17.7	5000	146	–	26	Yes
80	50 cs	25.0	40.1	17.8	5000	–	–	26	Yes
23	500 ms	25.2	39.8	–	5200	52	–	>126	Yes
44	500 ms	25.0	39.2	18.7	5000	47	–	>126	Yes
24	1000 ms	25.2	40.4	–	5100	323	–	–	Yes
51	500 gs	25.0	40.0	22.0	5000	29.3	–	>126	Yes
52	500 gs	25.0	40.6	21.0	5030	86	–	36	Yes
77	19g vs	25.0	42.1	17.5	5000	131	–	>126	Yes
17	50 ms	24.8	40.3	–	1300	23.1	–	–	Yes
45	None	30.1	40.3	19.0	5000	222	4.4	>126	Yes
76	None	30.1	39.6	21.0	10	653	4.4	>126	Yes

cient a from the starting conditions. For a given starting composition X_o, the exponential coefficient a increases with decreasing P_f, following a law of the form $\log_{10}a = B - AP_f$ (Fig. 5). The starting composition X_o affects markedly the intercept B: the coefficient B increases with increasing starting acetone content, but the slope A is only slightly sensitive to variations of starting composition. The values of the coefficient a can also be affected by the starting quantity of solution: the exponential coefficient a tends to increase with the initial mass of GRA solution M_o, all other parameters remaining unchanged (Fig. 6; Table 3). The GRA flow dynamics are weakly sensitive to the initial mass (a factor 2 or 3) compared to its sensitivity to composition or pressure (several orders of magnitude). The height reached by the flow and thus the exponential coefficient a must also be affected by the section of the shock-tube. The good overlap between our

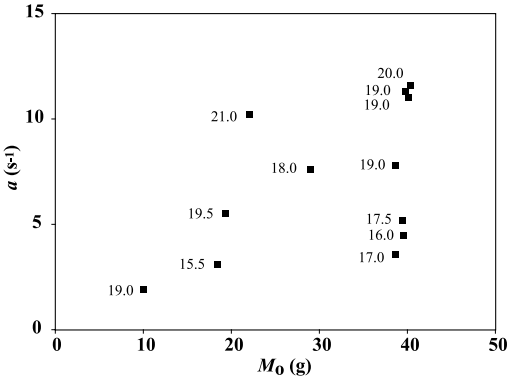

Fig. 6. Variation of the exponential coefficient a as a function of starting mass of solution M_o and temperature for runs starting with solutions containing 20 wt% acetone decompressed from 10^5 to 5000 Pa (Table 2). For each point, the temperature is given in °C.

Table 4
Properties of final GRA foam products

Run	X_o (wt%)	P_f (Pa)	X_f (wt%)	η_f (Pa.s)
70	20.1	5000	18.6	0.1
63	20.1	10	14.8	5.1
72	25.1	5000	17.4	1.8
73	25.1	10	8.5	647.6

The residual acetone content X_f in the foam at the top of the eruption column was measured after the decompression runs 70, 63, 72, that did not fragment and after run 73, that fragmented. The mean viscosity of the top foam products was calculated from their final composition, assuming room temperature (Table 3) and using the formula given in the caption of Table 2.

data compared to the data derived from Phillips et al. (1995) suggests that our use of about double the mass of solution (40 g vs. 16 g) compensates for the use of a test-cell with roughly double the surface of the section (4 cm vs. 2.6 cm diameter) to give comparable data.

In the more energetic runs the initial bubbly flow evolved into a flow of gas and fragments. The occurrence of fragmentation is inferred from the textures of the end-products. Fragmentation produced textures ranging from foamy slug flow to the spattering of the upper tube with fine fragments. In between these two extremes the final products consisted of a foam in the test-cell, an intermediate zone containing contorted cm-size fragments and the upper tube covered with elongated fines. Moreover, in some cases the instant of flow front fragmentation could be clearly identified on the frames. Fragmentation during a run was favoured by a high initial acetone content and a low final pressure. GRA solutions containing from 15 to 20 wt% acetone generated only bubbly flows. GRA solutions containing 25 wt% did not fragment after decompression down to 5000 Pa but fragmented at 10 Pa. GRA solutions containing 30 wt% fragmented at higher pressure, when decompressed to $P_f \leq 5000$ Pa. The dataset for the pure GRA system implies that fragmentation occurs in flows that reach a critical value of the exponential coefficient a in the initial bubbly flow of between 110 and 212 s^{-1} (Fig. 5; Table 3).

The less energetic runs produced only a bubbly flow and ended with a static foam with a rounded top surface. When the low pressure was maintained for a few minutes, the crust of the foam tended to crack locally. The evolution of the properties of the front of the GRA bubbly flows is strongly dependent on the run conditions. In non-fragmenting runs, high initial acetone contents and low final pressures lead to more degassed final top foams. The extent of the degassing of the final top foam can be inferred by both qualitative observation and measurement. Qualitatively, less degassed foams were 'wetter'; they were sticky to the touch and prone to collapse, i.e. they were more inclined to flow under their own weight. By contrast, more degassed foams were 'dryer', stronger and did not appear to flow at all, i.e. they were generally more like solids. The transition from 'wet' to 'dry' was seen to be progressive. Determination of the residual acetone content in the foams after a run provides a direct measure of the final degassed state (see Table 4). The implication from these qualitative and quantitative observations is that, in the non-fragmenting flows, the viscosity of the liquid in the final top foam increases with increasing initial acetone content and decreasing final pressure.

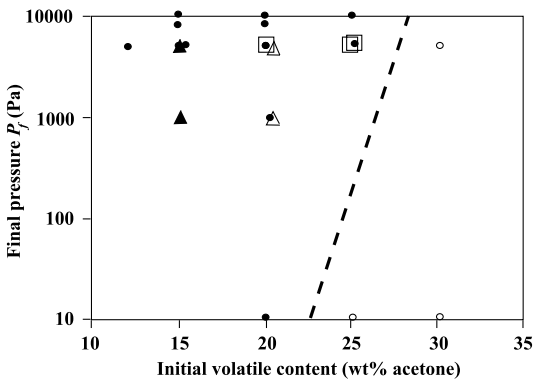

Fig. 7. Critical fragmentation conditions as a function of initial acetone content and final pressure. The hollowed symbols are for fragmenting runs and the full symbols for non-fragmenting runs. The bubble and particle-free runs are shown as spheres, the bubble-bearing runs as triangles and particle-bearing runs (with 500 mustard seeds) as squares. The critical conditions for flow fragmentation in the pure GRA runs are shown by a dashed line. Fragmentation conditions are shifted towards lower initial acetone content and higher final pressure in both the bubble-bearing and the particle-bearing runs.

4.2. Effect of pre-existing bubbles

Six experiments were performed starting with solutions enriched in air bubbles. These solutions were prepared by vigorous stirring of the GRA solution before it was poured into the test-cell. The run was then performed without delay to limit the number of air bubbles escaping to the surface of the solution. The number density of air bubbles could not be measured before a run. Therefore, the results of the different runs are difficult to compare with each other. Despite the absence of precise quantitative data, the comparison between the bubble-bearing and the bubble- and particle-free runs is significant. Except in run 81, the propagation law of the flow remained in the exponential regime but the value of the exponential coefficient was significantly increased when the acetone content was 20 wt% (Table 3). The physical meaning of this result is discussed in Section 5.1. As a consequence of the energy increase of the initial bubbly flow in these runs compared to the pure GRA runs, the critical conditions for fragmentation were shifted towards lower acetone contents and lower amplitudes of decompression (Fig. 7). Fragmentation in bubble-enriched flows was observed with starting conditions that would not have led to fragmentation in bubble-free starting solutions. Run number 81 behaved in a distinct manner: in this experiment, the bubbly flow was characterised by a temporary propagation with a constant velocity of 80 mm s^{-1}.

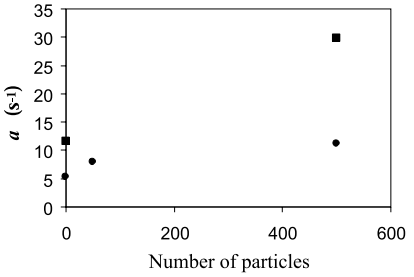

Fig. 8. Effect of the number density of particles on bubbly flow dynamics. Selection of runs with a starting acetone content of 20 wt% and a final pressure of 5000 Pa. The spheres represent runs without or with mustard seeds performed at a similar temperature of about 18°C: runs 49, 34 and 38. The squares represent runs without or with glass spheres performed at 20°C: runs 39 and 47.

4.3. Effect of solid particles

The addition of solid particles in suspension in the liquid was observed to induce marked changes in the bubbly flow dynamics compared to the bubble-free and particle-free runs. The effect was sensitive to the nature of the particles, their number density in the liquid and their spatial distribution (Table 3). The variation of the efficiency of vesiculation on the particles probably explains most of the difference between the effect of the different sinking particles. The bubbly flow dynamics were indeed unaffected in the case of silicon carbide particles that do not induce heterogeneous bubble nucleation: run 57 without particles and run 58 with 2 g of silicon carbide present similar bubbly flow dynamics. By contrast, bubbly flow dynamics were enhanced significantly (the exponential coefficient a increased) when the sinking particles provide efficient sites for heterogeneous bubble nucleation: mustard seeds and glass spheres, inducing shifted fragmentation conditions towards lower acetone contents and lower amplitudes of decompression (Table 3; Fig. 6).

The effect of the number density of particles depends on the starting conditions. The effect is minor for a starting acetone content of 15 wt% and a final pressure of 5000 Pa. For acetone contents of 20 and 25 wt%, the effect is significant and depends both on the number density of particles and on their nature. The increase in the number density of mustard seeds or glass spheres tends to result in more particles being incorporated into the flow and leads to an increase in the energy of the bubbly flow dynamics, even more efficiently in the case of the glass spheres (Fig. 8). This effect probably benefits slightly from the introduction of a few pre-existing internal air bubbles wetting the particles whose growth contributes to the flow in a similar way as in the runs with pre-existing bubbles described above. However, because the number of visible air bubbles on these particles is small, most of the effect probably comes from the growth of the numerous bubbles that nucleate heterogeneously on the particles. In some runs the bubbly flow dynamics were not exponential but characterised, at least temporarily, by a constant velocity. This relates

to runs 56, 59 and 80 which reached a plateau of constant velocity of about 3500, 3000 and 12 000 mm s^{-1}, respectively.

The spatial distribution of the particles in the starting solution can also affect the later flow dynamics. Indeed, the spatial distribution of particles constrains the spatial distribution of bubbles whose growth affects the flow dynamics. For example, when concentrated into a sinking layer, the particles had a little effect on the very early flow dynamics. The full development of the exponential expansion corresponds in general to the time when the bubbles that nucleated in the sinking layer of particles begin to reach the solution surface. If floating particles were present (coriander seeds or some seeds of the mixture of various seeds we used), an early pulse of flow front fragmentation was observed (runs 77, 78 and 80). This fragmentation process was short-lived and only concerned a limited volume of solution. A possible explanation for the observed bubbly flow dynamics is the local effect (in this case, on solution surface) of an increased number density of bubbles because these particles were located on the GRA nucleation surface, could be the site of heterogeneous bubble nucleation and were also characterised by a high efficiency of air bubble entrapment. The effect of the spatial distribution of bubbles on flow dynamics and the presence of various amounts of trapped air bubbles on particles are probably the main explanations for the dispersion in the data of exponential coefficients a measured in particle-bearing runs with similar starting conditions: compare runs 51 and 52 with glass spheres or runs 59, 89 and 77 using the same mixture of various seeds (Table 3).

5. Volcanological implications

5.1. Simulation of bubble growth and nucleation regime

The flow of magma out of a reservoir up to the surface is a dynamic and kinetic process and the final eruptive parameters depend on the whole ascent, decompression and degassing history of the magma in the conduit. Knowledge of the detailed flow dynamics is therefore the key to understanding the final dynamic conditions. Analogue experiments allow the flow dynamics of explosively vesiculating liquids to be studied directly. Various systems have been studied and it is clear that the flow dynamics observed are to some extent related to the characteristics of the specific analogue. In a constant diameter shock-tube, such as here, exsolution of CO_2 from an aqueous liquid produces flows characterised by constant acceleration (Mader et al., 1994) even if the viscosity of the liquid is increased up to 5 Pa.s by a polymer (Zhang et al., 1997; Zhang, 1998). However, it should be noted that the geometry and dimensions of the shock-tube can have a major impact on the dynamics. Experiments of large-scale eruptions from a spherical flask up a constant diameter tube reached quasi-steady flow conditions characterised by regular foamy slugs (Mader et al., 1997). The degassing of CO_2 resulting from the mixing and reaction of K_2CO_3 with HCl produces flows with a linear increase of acceleration (Mader et al., 1994, 1996). By contrast, the boiling of acetone from GRA solutions produces much more violent bubbly flows which are characterised by an exponential increase of acceleration (Mourtada-Bonnefoi and Mader, 2001). The reason for the differences in the dynamics of these flows resides in the kinetics of production of the gas phase and in the regime of bubble growth. Whilst none of the analogues is perfect, the GRA system is clearly a better analogue to magmatic degassing than previously used analogues because of its rheological properties.

However, a significant difference between the pure GRA system and magmas resides in the bubble nucleation process. Indeed, in the case of the GRA system, decompression of the pure (particle-free and bubble-free) liquid causes bubbles to nucleate only on the surface of the solutions; nucleation is ongoing during a run with a clear nucleation surface propagating down into the test fluid at constant velocity. By contrast, in the case of exsolving systems such as magmas, bubbles nucleate internally within the liquid above the nucleation depth either by homogeneous nucleation or by heterogeneous nucleation on crystals. The nucleation depth propagates downwards as material

is removed from the top. Additionally, bubble nucleation can occur as a quasi-instantaneous event, especially in the case of homogeneous bubble nucleation (Mourtada-Bonnefoi and Laporte, 1999; Mangan and Sisson, 2000), or as a continuous process in a context of microlite crystallisation (Simakin et al., 1999; Hammer et al., 1999).

In our experiments, we generated internal bubble nucleation by introducing air bubbles or particles into the starting GRA solutions. This brought the bubble nucleation and early growth behaviour of the analogue much closer to that of the natural system. The physics of bubble growth is governed by the competition between (1) gas expansion due to decompression, (2) diffusion of volatiles from the liquid phase into the bubbles, and (3) viscous resistance of the melt to bubble expansion. The observed exponential expansion of the GRA flows is probably the result of the quasi-constant nucleation rate of exponentially growing bubbles (Mourtada-Bonnefoi and Mader, 2001). Exponential bubble growth can be interpreted as due to a diffusion-driven but viscosity-limited bubble growth regime (Navon et al., 1998; Mourtada-Bonnefoi and Mader, 2001) both in the pure GRA system and in the case of air bubble or particle-bearing runs. In the air-bubble bearing runs, the increase in the exponential coefficient compared to the pure GRA runs is probably caused by several factors. The rate of expansion will be enhanced by the decompression of the air bubbles themselves. Furthermore, diffusion will be enhanced because of the presence of these numerous centres for bubble growth and because the presence of air in the bubbles means that the partial pressure of acetone in them is low. In the particle-bearing runs, the main contribution to the flow occurs via continuous heterogeneous nucleation of bubbles on the particles. Also, the few air bubbles initially trapped on the solid particles contribute to the flow in the same way as in bubble-bearing runs.

5.2. Homogeneous and heterogeneous bubble nucleation

The comparison between particle-free and particle-bearing runs as well as the comparison between particle-bearing runs using floating and sinking particles demonstrate that the spatial distribution of early nucleated bubbles is crucial to the later flow in the GRA system. Firstly, runs with a bottom layer of a few sinking particles were characterised by early dynamics very similar to particle-free and bubble-free runs. On the other hand, runs with a layer of floating particles generated an early fragmentation pulse. The difference in response is due to the complex interplay of flow dynamics and bubble nucleation. The floating particles provided many nucleation sites ideally located to initiate vesiculation and also trapped a few air bubbles. Moreover, the particles were readily incorporated into the vesiculating flow adding to the ease of ongoing nucleation. Additionally, the number density of bubbles produced by nucleation is a controlling factor of the energy of the resulting GRA bubbly flow dynamics.

In nature, the spatial distribution and the nucleation rate of bubbles in an erupting magma is mainly controlled by the kinetics of homogeneous bubble nucleation and heterogeneous bubble nucleation on crystals. Few quantitative data are to-date available on the kinetics of homogeneous and heterogeneous bubble nucleation (Hurwitz and Navon, 1994; Navon et al., 1998; Mourtada-Bonnefoi and Laporte, 1999; Mangan and Sisson, 2000; Mourtada-Bonnefoi and Laporte, 2002). The existing data suggest that both phenomena may take place and that their relative efficiency to generate bubbles might be very variable in magmas depending on pre-eruptive volatile content and crystal nature, number density and surface properties. Our experimental results using the GRA system suggest the acquisition of additional data on the distribution of crystals and their facility to induce heterogeneous bubble nucleation in magmas could help to constrain magma flow dynamics.

5.3. Magma fragmentation mechanism

The physics of magma fragmentation is poorly understood. It is quite probable that both ductile and brittle mechanisms occur within magmatic systems due to the enormously wide range of vis-

cosity and dynamical regime that they encompass. Ductile and brittle fragmentation probably proceed via distinct mechanisms and the question of the transition between these two extremes is a subject of debate (Dingwell, 1997). From a theoretical point of view the problem is to define the critical physical condition for fragmentation. In the case of ductile fragmentation, Proussevitch et al. (1993) propose a criterion based on a critical thickness of the films or plateau borders within the foam. In the case of brittle fragmentation the criterion is a pressure threshold to be overtaken by the product of the viscosity of the mixture and its strain rate (Barmin and Melnik, 1993; Papale, 1999; Melnik, 1999).

Our analogue experiments provide data to discuss the fragmentation mechanism. The low starting viscosity of our analogue solutions but the high viscosity of pure gum rosin suggest the dynamic fragmentation mechanism in the GRA system might range from ductile to brittle fragmentation depending on run conditions. The extreme elongation and contortion of the fragments indicate a low mean viscosity at fragmentation. This observation is suggestive of ductile fragmentation. However, the strength of the fragments indicates the existence of highly-degassed and viscous films around bubbles (Mourtada-Bonnefoi and Mader, 2001). As a consequence, GRA fragmentation may locally involve the brittle rupture of highly viscous bubble walls. The fragmentation process of GRA bubbly flows is thus probably neither entirely ductile nor entirely brittle. We suggest this might also be true for magmas fragmenting in a volcanic conduit. The production of contorted and extremely elongated volcanic fragments is thus not sufficient to infer a purely ductile fragmentation mechanism.

5.4. Magma fragmentation conditions

The magma fragmentation criterion is crucial to the accurate prediction of explosive vs. effusive flow regime. Our experimental conditions produced both non-fragmenting and fragmenting flows that can be taken as analogous to effusive and explosive volcanism, respectively. The experiments demonstrate that magmas of similar composition and volatile content may display a wide range of fragmentation behaviour for a fixed geometry and dimension of the conduit. Variations in crystallinity of the erupting magma and the involvement of a separate pre-existing gas phase from the storage zone can control the fragmentation conditions. The effect of crystals in suspension in the magma on fragmentation conditions probably derives from a combination of several phenomena. Firstly, the enhancement of vesiculation kinetics via heterogeneous bubble nucleation on crystals produces a more energetic bubbly flow dynamics. Secondly, regardless of their efficiency for heterogeneous bubble nucleation, crystals affect the fragmentation threshold: they ease ductile fragmentation (Proussevitch et al., 1993) but delay brittle fragmentation (Martel et al., 2001). A possible consequence for the reverse effect of crystals on bubbly flow dynamics and on brittle fragmentation conditions is the observation in nature of pumices showing a positive (e.g. Jurado-Chiray and Walker, 2001) but also a negative correlation between crystallinity and vesicularity (e.g. Klug and Cashman, 1994). We conclude that the physics of the entrainment of crystals and gas bubbles out of the chamber into the conduit have clear implications for the evolving flow regime and the ultimate fragmentation behaviour.

Acknowledgements

This work was supported by the EC-Network project ENV4-0703. We thank Fred Wheeler and Mike Dury for technical assistance with the building of the shock-tube. Thanks are due also to Jon Blower for providing the measurements of acetone diffusivity in gum rosin–acetone solutions. Helpful reviews by Takehiro Koyaguchi and two anonymous reviewers have led to considerable improvements.

References

Alibidirov, M.A., Dingwell, D.B., 1996a. An experimental facility for the investigation of magma fragmentation by rapid decompression. Bull. Volcanol. 58, 411–416.

Alibidirov, M.A., Dingwell, D.B., 1996b. Magma fragmentation by rapid decompression. Nature 380, 146–148.

Barmin, A.A., Melnik, O.E., 1993. Eruption dynamics of high-viscosity gas-saturated magmas. Izv. Ros. Akad. Nauk. Mekh. Zhidk. Gaza 2, 49–60.

Blower, J.D., 2001. Degassing Processes in Volcanic Eruptions. Ph.D. Thesis, University of Bristol.

Blower, J.D., Keating, J.P., Mader, H.M., Phillips, J.C., 2001a. Inferring volcanic degassing processes from vesicle size distributions. Geophys. Res. Lett. 28, 347–350.

Blower, J.D., Mader, H.M., Wilson, S.D.R., 2001b. Coupling of viscous and diffusive controls on bubble growth during explosive volcanic eruptions. Earth Planet. Sci. Lett. 193, 47–56.

Blower, J.D., Keating, J.P., Mader, H.M., Phillips, J.C., 2002. The evolution of bubble size distributions in volcanic eruptions. J. Volcanol. Geotherm. Res. 120, 1–23.

Cobbold, P.R., Jackson, M.P.A., 1992. Gum rosin (colophony): A suitable material for thermomechanical modelling of the lithosphere. Tectonophysics 210, 255–271.

Dingwell, D.B., 1997. The brittle–ductile transition in high-level granitic magmas: Material constraints. J. Petrol. 38, 1635–1644.

Hammer, J.E., Cashman, K.V., Hoblitt, R.P., Newman, S., 1999. Degassing and microlite crystallization during pre-climactic events of the 1991 eruption of Mt. Pinatubo, Phillipines. Bull. Volcanol. 60, 355–380.

Hill, L.G., Sturtevant, B., 1990. An experimental study of evaporation waves in a superheated liquid. In: Meier, G.E.A., Thompson, P.A. (Eds.), Adiabatic Waves in Liquid-Vapor Systems.

Hurwitz, S., Navon, O., 1994. Bubble nucleation in rhyolitic melts: Experiments at high pressure, temperature and water contents. Earth Planet. Sci. Lett. 122, 267–280.

Jurado-Chiray, Z., Walker, G.P.L., 2001. Variability of plinian fall deposits: Examples from Okataina Volcanic Centre, New Zealand. J. Volcanol. Geotherm. Res. 111, 239–263.

Klug, C., Cashman, K.V., 1994. Vesiculation of May 18, 1980, Mount St. Helens magma. Geology 22, 468–472.

Lensky, N.G., Lyakhovsky, V., Navon, O., 2001. Radial variations of melt visosity around growing bubbles and gas overpressure in vesiculating magmas. Earth Planet. Sci. Lett. 186, 1–6.

Mader, H.M., Zhang, Y., Phillips, J.C., Sparks, R.S.J., Sturtevant, B., Stolper, E., 1994. Experimental simulations of explosive degassing magma. Nature 372, 85–88.

Mader, H.M., Phillips, J.C., Sparks, R.S.J., Sturtevant, B., 1996. Dynamics of explosive degassing in magma: Observations of fragmenting two-phase flows. J. Geophys. Res. 101, 5547–5560.

Mader, H.M., Brodsky, E.E., Howard, D., Sturtevant, B., 1997. Laboratory simulations of sustained volcanic eruptions. Nature 388, 462–464.

Mangan, M., Sisson, T., 2000. Delayed, disequilibrium degassing in rhyolite magma: Decompression experiments and implications for explosive volcanism. Earth Planet. Sci. Lett. 183, 441–455.

Martel, C., Dingwell, D.B., Spieler, O., Pichavant, M., Wilke, M., 2000. Fragmentation of foamed silicic melts: An experimental study. Earth Planet. Sci. Lett. 178, 47–58.

Martel, C., Dingwell, D.B., Spieler, O., Pichavant, M., Wilke, M., 2001. Experimental fragmentation of crystal- and vesicle-bearing silicic melts. Bull. Volcanol. 63, 398–405.

Melnik, O.E., 1999. Fragmenting magma. Nature 397, 394–395.

Mourtada-Bonnefoi, C.C., Mader, H.M., 2001. On the development of highly-viscous skins of liquid around bubbles during magmatic degassing. Geophys. Res. Lett. 28, 1647–1650.

Mourtada-Bonnefoi, C.C., Laporte, D., 1999. Experimental study of homogeneous bubble nucleation in rhyolitic magmas. Geophys. Res. Lett. 26, 3505–3508.

Mourtada-Bonnefoi, C.C., Laporte, D., 2002. Homogeneous bubble nucleation in rhyolitic magmas: An experimental study of the effect of H_2O and CO_2. J. Geophys. Res. 107, 1–21.

Navon, O., Chekhmir, A., Lyakhovsky, V., 1998. Bubble growth in highly viscous melts: Theory, experiments, and autoexplosivity of dome lavas. Earth Planet. Sci. Lett. 160, 763–776.

Papale, P., 1999. Strain-induced magma fragmentation in explosive eruptions. Nature 397, 425–428.

Phillips, J.C., Lane, S.J., Lejeune, A.-M., Hilton, M., 1995. Gum rosin–acetone system as an analogue to the degassing behaviour of hydrated magmas. Bull. Volcanol. 57, 263–268.

Proussevitch, A.A., Sahagian, D.L., Kutolin, V.A., 1993. Stability of foams in silicate melts. J. Volcanol. Geotherm. Res. 59, 161–178.

Proussevitch, A.A., Sahagian, D.L., 1998. Dynamics and energetics of bubble growth in magmas: Analytical formulation and numerical modelling. J. Geophys. Res. 103, 18223–18251.

Sahagian, D.L., 1999. Magma fragmentation in eruptions. Nature 402, 589–591.

Shaw, H.R., 1963. Obsidian–H_2O viscosities at 1000 and 2000 bars in the temperature range 700°C to 900°C. J. Geophys.Res. 68, 6337–6343.

Simakin, A.G., Armienti, P., Epel'baum, M.B., 1999. Coupled degassing and crystallization: Experimental study at continuous pressure drop, with application to volcanic bombs. Bull. Volcanol. 61, 275–287.

Sugioka, I., Bursik, M., 1995. Explosive fragmentation of erupting magma. Nature 373, 689–692.

Zhang, Y., Sturtevant, B., Stolper, E.M., 1997. Dynamics of gas-driven eruptions: Experimental simulations using CO_2–H_2O-polymer system. J. Geophys. Res. 102, 3077–3096.

Zhang, Y., 1998. Experimental simulations of gas-driven eruptions: Kinetics of bubble growth and effect of geometry. Bull. Volcanol. 59, 281–290.

Zhang, Y., 1999. A criterion for the fragmentation of bubbly magma based on brittle failure theory. Nature 402, 648–650.